Chem Soc Rev

RSCPublishing

REVIEW ARTICLE

Nanostructured hydrotreating catalysts for electrochemical hydrogen evolution

Cite this: DOI: 10.1039/x0xx00000x

Carlos G. Morales-Guio, Lucas-Alexandre Stern, and Xile Hu*

Received 00th January 2012,
Accepted 00th January 2012

DOI: 10.1039/x0xx00000x

www.rsc.org/

Progress in catalysis is driven by society's needs. The development of new electrocatalysts to make renewable and clean fuels from abundant and easily accessible resources is among the most challenging and demanding tasks for today's scientist and engineers. The electrochemical splitting of water into hydrogen and oxygen has been known for over 200 years, but in the last decade and motivated by the perspective of solar hydrogen production, new catalysts made of earth-abundant materials have emerged. Here we present an overview of recent developments of the non-noble metal catalysts for electrochemical hydrogen evolution reaction (HER). Emphasis is given to the nanostructuring of industrially relevant hydrotreating catalysts as potential HER electrocatalysts. The new syntheses and nanostructuring approaches might pave the way to future developments of highly efficient catalysts for energy conversion.

1. Introduction

Molecular hydrogen (H_2) has been considered as an energy carrier since the beginning of the 1970's.[1] A hydrogen fuel community has been imagined where excess energy from renewable sources is not fed into the grid, but stored in the form of H_2 to be later transformed to electricity, used directly as fuel, or used as pillar to sustain a future "methanol economy".[2, 3] The implementation of H_2 as energy carrier is desirable because it is the molecule with the highest energy density per unit of mass, and when combusted in an engine or transformed into electricity in a fuel cell, it produces only water as the byproduct. In comparison, carbon-based fuels produce water and CO_2.

Although hydrogen is the most abundant element on earth, it does not exist as a free molecule, and consequently, efficient and sustainable H_2 production technologies are required. Today, most H_2 is produced from fossil resources through a steam reforming process where steam reacts with hydrocarbons to give H_2 and CO_2.[4] This H_2 production method consumes fossil fuels and still emits CO_2. A clean and renewable method of H_2 production is electrolysis of water using renewable energies, in particular solar energy (forward direction in Scheme 1).[5, 6] The electrochemical water splitting, first observed in 1789,[7, 8] is divided in two half-cell reactions: the hydrogen evolution reaction (HER) and the oxygen evolution reaction (OER). Both HER and OER require catalysts to lower the electrochemical overpotential (overpotential is the difference between the applied and thermodynamic potentials of a given electrochemical reaction). Platinum group metals are the most efficient catalysts for HER, capable of driving significant currents close to the thermodynamic potential. However, these noble metals are among the least abundant elements on Earth and are not sufficiently present to catalyse HER at a scale comparable to the global energy demand.

$$H_2O + \text{energy} \leftrightarrows H_2 + 0.5\ O_2$$

Scheme 1 Forward reaction: splitting of water into hydrogen and oxygen using energy from renewable sources. Reverse direction: production of energy on demand through combination of H_2 and O_2.

This review summarizes the development of heterogeneous catalysts made entirely of earth-abundant elements for electrochemical HER. Similar to other heterogeneous catalysts, the performance of HER catalysts is limited by the density and reactivity of active sites. Furthermore, poor electron transport, low surface area and instability under operating conditions are common pitfalls of these electrocatalysts.[9-11] During the last decade, however, significant improvements in efficiency have been achieved through the design of nanostructured catalysts that either expose preferentially the most active reaction sites, or electronically connect a higher number of these sites to the back contact electrode, or both. This strategy is widely applied to catalysts previously used for the hydrotreating (HDT) of crude petroleum products.

We will first describe the basic mechanistic considerations of HER, followed by an introduction to hydrotreating catalysts.

We will then describe how nanostructuring of known hydrotreating catalysts has led to the preparation of increasingly efficient hydrogen evolution electrocatalysts. The review does not cover the work on using earth abundant materials as supports or co-catalysts for Pt group metals.

Despite the fact that the earth-abundant HER catalysts developed thus far have not reached the same efficiency exhibited by Pt, the nanostructuring strategies summarized here provide a valuable approach for catalyst optimization and may lead to a future breakthrough in catalyst development, not only for HER, but also for other important chemical reactions.

1.1 Electrochemical HER

Water splitting consists of both OER (eqn (1)) and HER (eqn (2)).

$$2H_2O\ (l) \rightarrow O_2\ (g) + 4H^+\ (aq) + 4e^- \quad (1)$$

$$2H^+\ (aq) + 2e^- \rightarrow H_2\ (g) \quad (2)$$

The free energy change (ΔG^0) for the conversion of one molecule of water into hydrogen and oxygen (Scheme 1) under standard temperature and pressure (STP) conditions is +237.2 kJ per mol of H_2. However, extra work is required to expand the gases produced ($T\Delta S^0$), and when this is taken into account, the enthalpy change ($\Delta H^0 = \Delta G^0 + T\Delta S^0$) is +286 kJ per mol of H_2. These values correspond to a reversible electrolysis cell voltage of $\Delta E^0_{rev,298}$ = 1.23V and a thermoneutral (heat is not lost or required) cell voltage of $\Delta E^0_{th,298}$ = 1.48V for water splitting. In the ideal case, where $T\Delta S^0$ is supplied by an external source, the application of only 1.23V of external potential would be sufficient to start water splitting in an electrochemical cell. In practice, water electrolysis is less efficient and external potentials well above the thermodynamic minimum value of 1.23V are required. Overpotentials are essential to drive the electron transfer processes at significant rates and to overcome the kinetic barriers imposed by the high activation energies for the formation of reaction intermediates on the surface of the electrode. Efficient electrocatalysts are materials that lower these overpotentials.

1.2 Mechanism of HER

HER is a multi-step process taking place on the surface of an electrode. The first step of HER is the Volmer or *discharge* reaction (blue arrows in Fig. 1). In this step, an electron transfer to the electrode is coupled to a proton adsorption on an empty active site of the electrode to yield an absorbed hydrogen atom. In acidic electrolytes the proton source is the hydronium cation (H_3O^+); in alkaline solutions, it is the water molecule. Discharge of water in acid is improbable.[12] Subsequently H_2 formation may occur via two different reaction pathways. In one possibility, the transfer of a second electron to the absorbed hydrogen atom is coupled to the transfer of another proton from the solution to evolve H_2. This process is shown with purple arrows in Fig. 1 and is the so-called Heyrovsky or *ion+atom* reaction. In another possibility, which was confirmed for Pt, two absorbed hydrogen atoms combine on the surface of the electrode to give H_2, in the so-called Tafel or *combination* reaction (red arrows in Fig. 1).

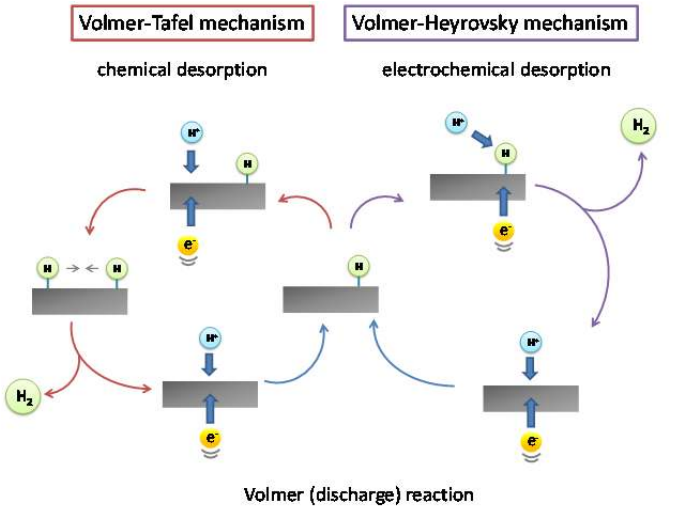

Fig. 1 The mechanism of hydrogen evolution on the surface of an electrode in acidic solutions.

Tafel slopes are commonly used to discern the predominant HER mechanism.[13] Tafel slopes indicate the potential difference necessary to increase or decrease the current density by 10-fold. The Tafel slopes have been derived theoretically from the Butler-Volmer equation for three limiting cases.[14] (1) If the discharge reaction is fast and H_2 is evolved by a rate-determining combination reaction, a slope of 2.3RT/2F, that is, 29 mV dec^{-1} at 25°C should be observed. (2) If the discharge reaction is fast and H_2 is evolved by a rate determining *ion+atom* reaction, the Tafel slope should be 4.6RT/3F, that is, 38 mV dec^{-1} at 25°C. (3) If the discharge reaction is slow, then regardless whether H_2 is evolved by the combination reaction or the *ion+atom* reaction, the Tafel slope should be 4.6RT/F, that is, 116 mV dec^{-1} at 25°C.

The exchange current density (j_0) is another important kinetic parameter in electrocatalysis that is correlated to the rate of electron transfer under reversible conditions (that is, at zero overpotential). The magnitude of the exchange current density influences the rate of the electrochemical reaction at other potentials. The Tafel equation can be used to describe the current-potential relation at a significant overpotential (η):

$$\eta = b \log(j/j_0) \quad (3)$$

where j is the current density, j_0 is the exchange current density and b is the Tafel slope.

Ideal catalysts have low Tafel slopes and high exchange current densities. In reality, however, one sometimes has to compare a

catalyst with a high exchange current density but also a high Tafel slope with another catalyst with a lower exchange current density but also a smaller Tafel slope. Which catalyst is better depends on the targeted current density. Let's take as an example two catalyst, one with an exchange current density of 10^{-4} A cm^{-2} and a Tafel slope of 100 mV dec^{-1}, and the other with a lower exchange current density of 10^{-6} A cm^{-2} but a Tafel slope of 40 mV dec^{-1}. To achieve a current density of 10 mA cm^{-2}, the former catalyst requires 200 mV of overpotential, while the latter requires only 160 mV. The latter catalyst is therefore a better catalyst for this application. In comparison, Pt has an exchange current density in the order of 10^{-3} A cm^{-2} and a Tafel slope of 30 mV dec^{-1} for HER. Therefore, a current density of 10 mA cm^{-2} can be reached with an overpotential of only 30 mV.

Fig. 1 shows that hydrogen evolution takes place through an absorbed hydrogen intermediate. The Gibbs free energy for hydrogen adsorption (ΔG_{H^*}) on a metal has been proposed to be a good descriptor of the intrinsic activity of a metal for HER.[15-18] A plot of exchange current densities against ΔG_{H^*} has a volcano shape. Pt group metals are at the summit of the volcano, having the highest activity and close to zero hydrogen absorption energy (Fig. 2).

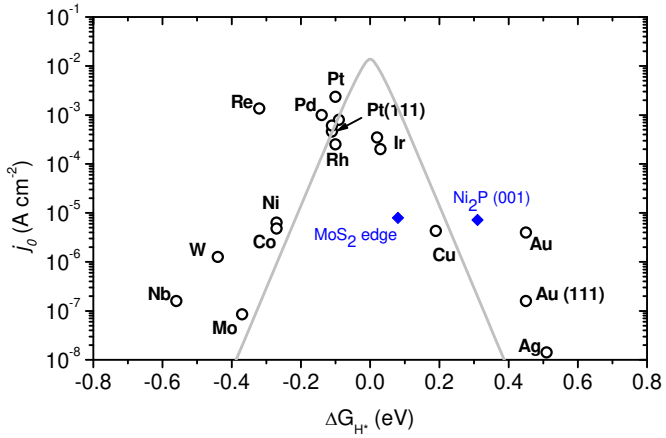

Fig. 2. A Volcano plot of experimentally measured exchange current density as a function of the DFT-calculated Gibbs free energy of adsorbed atomic hydrogen. The simple kinetic model proposed by Norskov and co-workers to explain the origin of the volcano plot is shown as the solid lines.[15]

The volcano plot reflects the Sabatier principle. Metals to the left of Pt bind hydrogen atoms too strongly, blocking the active site and failing to evolve hydrogen. On the other hand, metals to the right of Pt binds hydrogen too weakly, failing to stabilize the intermediate state and preventing any reaction from taking place. Quantum chemical calculations showed that ΔG_{H^*} is a good descriptor of materials that can catalyse HER and applies not only to pure metals, but also alloys, enzymes and transition metal compounds.[16, 18] Fig. 2 shows the edge site of MoS_2 which has a modest ΔG_{H^*} and a high activity for HER. A good deal of work has been done to prepare MoS_2 materials rich in these edge sites, which is a major subject of this review. The adsorption free energy of hydrogen on the Ni_2P (001) surface has also been calculated by DFT to be 0.31 eV[19] and recently a turn over frequency (TOF) of 0.015 s^{-1} was estimated at η = 100 mV for an active Ni_2P HER electrocatalyst.[20] The measured TOF is equivalent to an exchange current density of $j_0 = 7.2\text{x}10^{-6}$ A cm^{-2}, assuming an active site density of $1.5\text{x}10^{15}$ site cm^{-2}.

The activity of an electrocatalyst is often expressed as a given current density at a given overpotential. In addition to the intrinsic activity which is related to TOF, the current density also depends on the loading of catalyst per area and the density of active sites. However, the effect of catalyst loading is not considered here.

1.3 Hydrotreating

Hydrotreating (HDT) or hydroprocessing refers to a variety of catalytic hydrogenation processes where heteroatoms (S, N, O or metals) are removed from natural gas and petroleum products in refineries. Depending on the atom removed, these processes are called hydrodesulfurization (HDS), hydrodenitrogenation (HDN), hydrodeoxygenation (HDO) and hydrodemetallization (HDM). Hydrotreating is one of the most important catalytic processes and its annual sales are close to 10% of the total world market for catalysts.[21] Environmental concerns are forcing drastic changes in motor fuel specifications with regulations becoming increasingly stringent to minimize SO_x and NO_x emissions. At the same time, the quality of future crude oil feedstock is expected to deteriorate due to the lower availability of light petroleum. Therefore, technically less satisfactory heavy feedstock will soon be used for the production of liquid fuels. These factors have driven the growth of the HDT catalyst market and motivated further research of more active catalysts.

Among the various catalysts used in HDT processes, supported metal sulphides are the most important and most studied. Standard industrial HDT catalysts are composed of molybdenum sulphide (or tungsten sulphide) phase-promoted by cobalt or nickel and are usually supported on alumina.[21] Other important HDS catalysts are metal carbides (e.g. β–Mo_2C) and more recently metal phosphides (i.e. Ni_2P) have shown a potential for HDS.[22]

Although hydrotreating processes have been used for almost 80 years, just recently a detailed understanding of the process chemistry and catalyst structure has arrived. The application of modern analytical techniques such as transmission electron microscopy (TEM), scanning tunnelling microscopy (STM), together with the development of computational tools based on density functional theory (DFT) have closed the gap between underlying science and the catalyst technology.[21, 23, 24] Surface science experiments give valuable information on the morphology of catalysts and their active sites and provide a quantitative description of a range of surface phenomena.[24, 25] For example, high-resolution STEM analysis was used to

determine the atomic-scale structure of the catalytically important edges of the industrially relevant graphite-supported MoS_2 nanocatalyst.[26] Analysis of high-resolution STEM images such as the one shown in Fig. 3a reveals that the Mo edge is terminated with single S atoms (1S) and that the Mo edge is not just a simple truncation of the bulk MoS_2 structure. This observation is consistent with previous STM and DFT studies. The Mo-edge termination with a single S atom matches that of the 50% sulphur covered Mo edge previously observed in model catalysts and predicted by DFT(Fig. 3b). Furthermore, these studies confirm that the low-indexed edges are indeed present under catalytically relevant conditions and are the active sites for HDS.[26, 27]

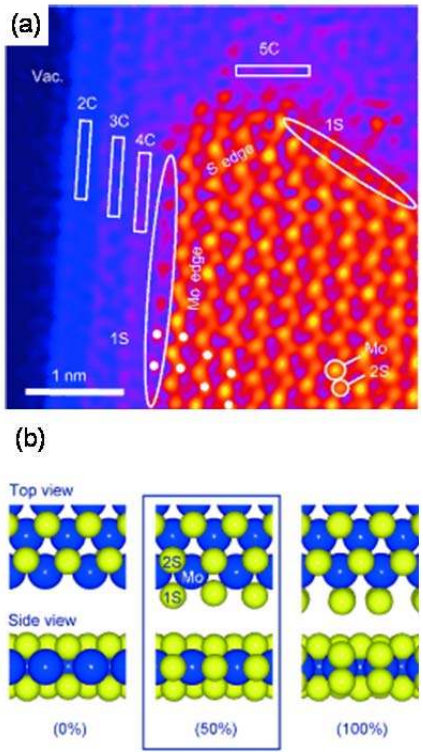

Fig. 3 (a) High-resolution STEM image of a single-layer MoS_2 nanocrystal on a graphite support. White dots superimposed on the image denote sulphur sublattice (2S) positions of the MoS_2 basal plane and Mo edge. The image of this industrial-style MoS_2 nanocatalysts shows that the Mo edge is not just a simple truncation of the bulk MoS_2 structure, which is an observation consistent with the DFT model. (b) Ball models (top and side views, respectively) of different S coverage levels at the Mo edge (0%, 50%, 100%). Adapted with permission from ref. 26, copyright 2011, Wiley-VCH.

The knowledge acquired during the study of HDS catalysts is beneficial for the development of HER catalysts, as described later. In the time being, it is important to note that the Mo-edge sites that are active for HDS have been proposed as the active sites for HER by MoS_2.

1.4 Relation between HDT and HER

Both HDT and HER involve adsorbed hydrogen atom as an intermediate, thus, they impose similar requirement for the binding energy of hydrogen on surfaces. Volcano plots of activity as function of ΔG_{H^*} have been found for HDT,[28, 29] similar to HER. On the other hand, HDT and HER also involve different processes. In HDT, organic molecules need to be absorbed and activated; in HER, chemical reactions are coupled to electron transfers on the electrode. Thus, a good HDT catalyst is not necessarily a good HER catalyst. However, good HDT catalysts should be logical candidates in the initial screening of HER catalysts. This review highlights the catalysts that are positive hits in this screening and that are further optimized by nanostructuring to meet the specific requisites of HER.

2. Nanostructuring of HDT catalysts for HER

2.1 MoS_2 and WS_2

MoS_2 and WS_2 are long-known catalysts for hydrodesulfurization. Recent studies have shown that nanostructured MoS_2 and WS_2 are promising electrocatalysts for HER even though the bulk materials are poor catalysts.[30-32] Two perspectives by our group and the group of Chorkendorff have summarized the chronological development of this area until the end of 2011.[9, 10] Briefly, initial studies were done by Tribusch *et al.* in 1970s on the electrochemistry and photochemistry of MoS_2 layered crystals,[33] but it was not until Nørskov, Chorkendorff, and co-workers showed in 2005 that the edge sites of MoS_2 have a good HER activity that interest in this type of materials as HER catalysts spurred.[16] In that seminal work, Mo-edge sites were identified as active sites for HER; the theoretical free energy of adsorption of hydrogen on this metallic edge is similar to those of Pt and the active sites of hydrogenases. This was followed by a study that made use of model MoS_2 catalysts with controlled size and morphology. The study showed that the exchange current density of MoS_2 nanocrystals is proportional to the length of edges sites but not to the basal areas in truncated MoS_2 hexagons. Such study confirmed that the edge site is the catalytically active for HER.[30] Since then, various material and electrode preparation methods have been reported for the optimization of MoS_2 catalysts. Five main approaches have been taken (i) increasing the surface area; (ii) increasing the number of active sites; (iii) improving the electrical contact from the back contact to the active sites; (iv) exfoliation of layered MoS_2 and WS_2; (v) modification of the catalytic reactivity of the MoS_2 edge by substitution with transition metals such as Co or Ni to form bimetallic catalytic sites. Approaches (i) to (iv) aim to increase the number of electronically connected active sites per unit of geometric area; the goal is to increase exchange current density and move upward in the volcano plot shown in Fig. 2. The last approach aims to reduce the intrinsic free energy of adsorption of hydrogen on the active site; the goal is to move a catalyst horizontally towards the middle of the volcano plot. This last approach is beyond the scope of this review, so it will only be mentioned when coupled to a nanostructuring approach.

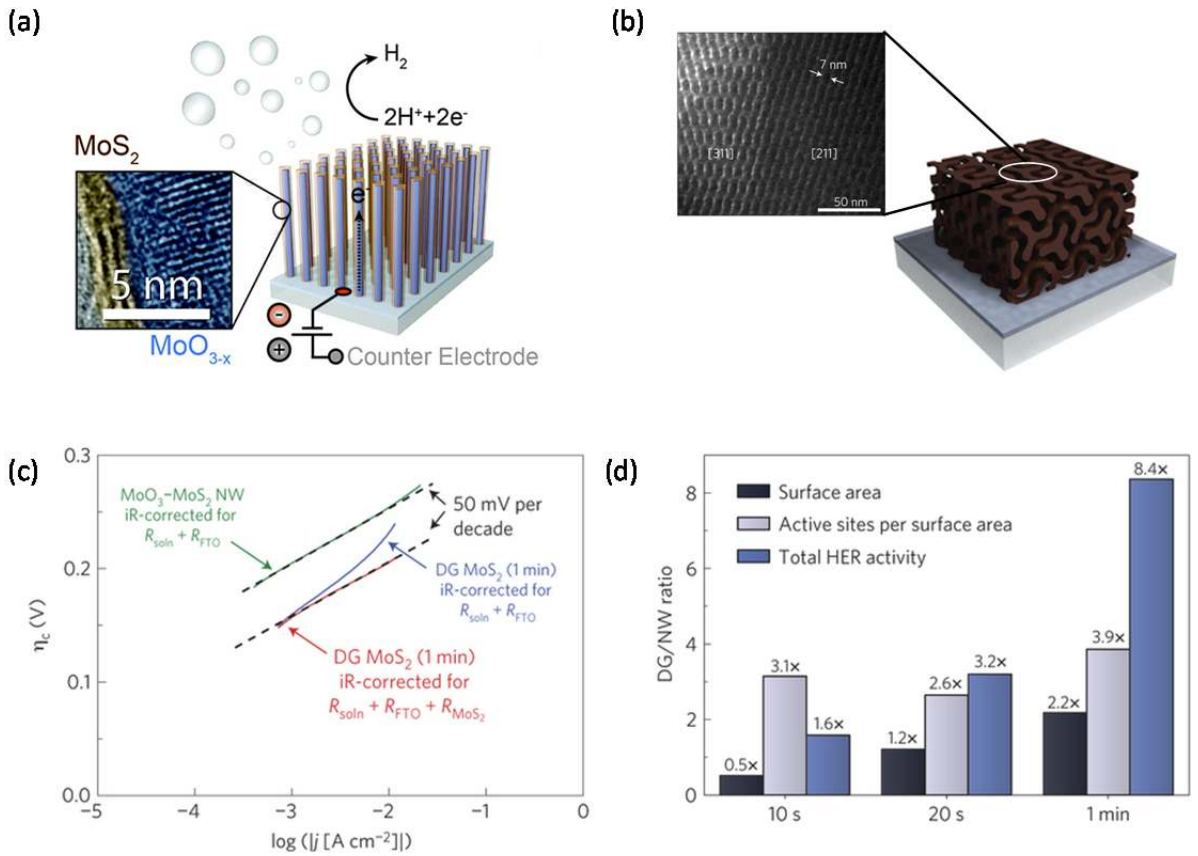

Fig. 4 (a) Schematic representation of MoO_3-MoS_2 core-shell nanowires (NW) for HER. Zoom in box: coloured TEM image of the internal morphology of the nanowire. Adapted with permission from ref. 34, copyright 2011, American Chemical Society. (b) Structural model of mesoporous MoS_2 with a double-gyroid (DG) morphology. Zoom in box: TEM image of double-gyroid MoS_2 where [311] and [211] projections of the double-gyroid structure are observed. The pore-to-pore distance is ~7 nm as indicated by the white arrows. (c) Tafel plot of double-gyroid MoS_2 (1min) versus core-shell MoO_3-MoS_2 nanowires, showing the 50 mV per decade Tafel slope (d) Ratios of surface area, density of active sites per surface area and total HER activity of the various double-gyroid MoS_2 films versus the nanowires. Figures (b)-(d) adapted with permission from ref. 35, copyright 2012, Nature Publishing Group.

A. Higher surface area electrodes. High-aspect ratio architectures have been used to improve the activity per geometric area and to maximize the diffusion of protons and molecular hydrogen. Jaramillo and co-workers reported that vertically-oriented core-shell nanowires (NW) produced by low-temperature sulfidization of MoO_3 nanowires have high activity for HER. A current density of 10 mA cm^{-2}, which corresponds to the photocurrent density expected for a 12% efficiency solar water splitting device, requires an overpotential of η_{10} = 250 mV. The Tafel slope is 50-60 mV dec^{-1} near the onset of current. The substoichiometric MoO_3 core provides a high aspect ratio template and enables facile charge transport, while the conformal MoS_2 shell provides excellent catalytic activity and protection against corrosion in strong acids.[34] The nanowires were stable over 10000 cycles of cycling stability test. Fig. 4a shows a schematic diagram of the core shell electrode. However, in this high-surface-area structure most of the MoS_2 basal planes were parallel to the nanowire axis as observed in the coloured TEM image shown in Fig. 4a, resulting in few edge sites exposed at the surface of the nanowires, limiting the HER activity of this electrode.

B. Higher surface area with preferential exposure of active edge sites. High-surface area alone is not sufficient if the density of catalytically active sites is low. To address this issue, Jaramillo and co-workers reported a synthetic method to produce a double-gyroid (DG) MoS_2 bicontinuos network with nanoscaled pores (Fig. 4b). This material preferentially exposed a large fraction of edge sites, which, together with its high surface area, leads to excellent activity for electrochemical HER.[35] Fig. 4c shows the comparison between these two high-surface area approaches. The DG structure shows a higher exchange current density compared to that of the nanowires but also an increased resistance to electron transfer. Variation of the electrode thickness with the electrodeposition time of the precursor (from 10 s to 1 min) shows that higher surface area electrodes can be obtained with longer times. More material is deposited and the template is filled. Independently of this, the number of active sites per surface area remains quiet constant as expected when using a nanostructured template with a constant surface to volume ratio throughout all the nanopores (Fig. 4d). Thanks to the higher surface area and the higher edge density, improvement in the total HER activity is observed.

However, MoS_2 is a semiconducting material and thicker films increased electron transport resistance, limiting the overall electrochemical performance at higher current densities. A current density of 10 mA cm^{-2} requires about 240 mV overpotential, similar to the core-shell MoO_3-MoS_2 NW electrode.

MoS_2 and $MoSe_2$ films with vertically aligned layers have also been synthesised through a kinetically controlled rapid growth method that preferentially exposes the thermodynamically less stable edge sites over terrace sites (Fig. 5).[36] The exchange current density measured has average values of 2.2 x 10^{-6} A cm^{-2} for MoS_2 and 2.0 x 10^{-6} A cm^{-2} for $MoSe_2$. The Tafel slopes are in the range of 105-120 mV dec^{-1}, indicating that the rate limiting step is the Volmer reaction. This material can be partially improved by tuning the substrate morphology and the choice of the material. This synthetic method has been extended to prepare first-row transition metal dichalcogenide[37] and $MoSe_2$ and WSe_2 catalysts for HER on curved and rough surfaces.[38]

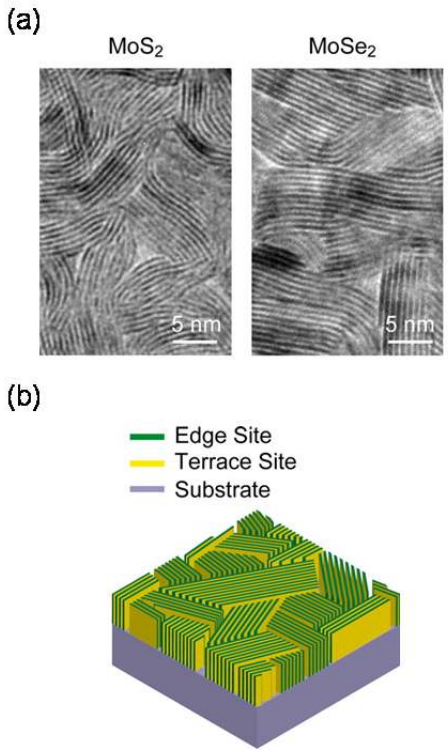

Fig. 5 (a) TEM images of MoS_2 and $MoSe_2$ films produced by rapid sulfurization, showing exposed edges. (b) Idealized structure of edge-terminated molybdenum chalcogenide fils with the layers aligned perpendicular to the substrate, exposing the edges of the layers. Adapted with permission from ref. 36, copyright 2013, American Chemical Society.

Two dimensional MoS_2 nanosheets (NS) with a high active site density were prepared through a microdomain reaction method.[39] The nanosheets were synthesized by ball-milling a mixture of MoO_3 and S_8, following by annealing at high temperatures. The MoS_2 NS possesses a high number of exposed edge sites and a thickness of only ca. 2 nm, leading to a high edge/basal ratio. The highest active site density was obtained for samples annealed at 550°C. The geometrical exchange current density is in the order of 10^{-5} A cm^{-2} and the tafel slope is 68 mV dec^{-1}. A current density of j = 10 mA cm^{-2} is reached at a 200 mV overpotential.

An alternative method to increase the number of active site is to introduce abundant defects on the basal planes during the preparation of MoS_2. This can lead to the cracking of the basal plane and subsequent exposure of additional active edge sites.[40] To obtain the defect-rich structure, an excess of thiourea was employed not only as a reducing agent for a heptamolybdate precursor, but also as an efficient additive to stabilize the resulting ultrathin nanosheets. The defect-rich MoS_2 ultrathin nanosheet displays a density of active sites that is 13 times higher than that of bulk MoS_2. Current densities as high as 13 mA cm^{-2} are obtained at 200 mV overpotential, with a Tafel slope of 50 mV dec^{-1}. Variation of the crystallization temperature showed that lower temperature facilitates the formation of oxygen-incorporated ultrathin nanosheets.[41] The nanosheets prepared at lower temperatures have an improved conductivity and exhibit simultaneously a high number of active sites and a good conductivity.[41] Current densities of j = 10 and 126 mA cm^{-2} are obtained at η = 180 and 300 mV, respectively. These current densities are among the highest for single-component MoS_2 electrocatalysts.

C. Nanostructuring of electrocatalyst supports to improve electron transport. While electron transport in the catalyst is a separate process from charge transfer reactions, it affects the global activity of a catalyst and is often reflected on high Tafel slopes. As MoS_2 is a semiconductor, the low conductivity of such catalysts might limit their catalytic performance. Our group show this is the case for several amorphous molybdenum sulphide catalysts.[42] Coupling MoS_2 with a highly conductive substrate should alleviate this problem.

Dai and co-workers reported a selective solvothermal synthesis of MoS_2 on reduced graphene oxide (RGO) sheets. The resulting MoS_2/RGO hybrid material consists of thin MoS_2 layers and a highly conductive underlying graphene network.[43] The coupling/interaction of MoS_2 with GO led to the selective growth of highly dispersed MoS_2 nanoparticles on GO. In strong contrast to aggregated MoS_2 particles grown freely in solution without GO, the MoS_2/RGO hybrid exhibited superior electrocatalytic HER activity relative to other MoS_2 catalysts (Fig. 6). A Tafel slope of ~41 mV dec^{-1} was obtained suggesting the Volmer-Heyrovsky mechanism for HER. j = 10 mA cm^{-2} is reached with only 140 mV of overpotential. The improved activity is partially due to the abundant and accessible edge sites of dispersed MoS_2. A second contribution comes from the enhanced electron transport by coupling graphene sheets to the less-conductive MoS_2 nanoparticles.

Our group prepared a hybrid catalyst system containing conductive carbon particles (Vulcan®) and amorphous MoS_3 particles. Compared to MoS_3 alone, the hybrid catalyst exhibited faster electron transport, manifested by a lower Tafel

slope (36 mV dec^{-1} instead of about 60 mV dec^{-1}) and the absence of a line-feature in the Nyquist plot of the impedance spectrum.[42] The latter was identified as a signature for slow electron transport in porous materials.

A facile hydrothermal method to deposit MoS_2 nanosheets on carbon nanotubes has also been reported.[44] The resulting MoS_2 shows good HER activity, likely due to coupling of MoS_2 to carbon nanotubes. WS_2 has also been grown on RGO in a one-pot hydrothermal reaction process at low temperature and show promising catalytic activity for HER.[45]

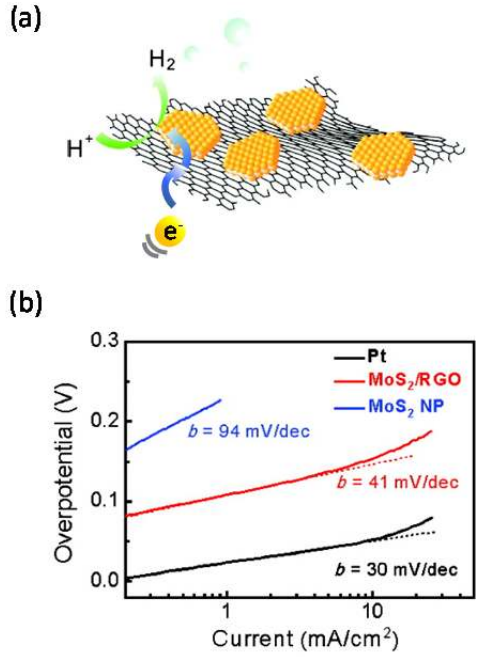

Fig. 6 (a) Structural model of MoS_2 nanoparticles on reduced graphene oxide (RGO) sheets. (b) Tafel plots recorded on glassy carbon electrodes with a catalyst loading of 0.28 mg cm^{-2}. Reprinted with permission from ref. 43, copyright 2011, American Chemical Society.

D. Exfoliation of MoS_2 and WS_2.

Liquid exfoliation of bulk MoS_2 has been proposed as a nanostructuring approach.[46-48] Ultrasmall molybdenum disulphide nanoparticles with diameters of 1.47 ± 0.16 nm were fabricated from bulk MoS_2 by a combination of ultrasonication and centrifugation. Self-assembly of these ultrasmall nanoparticles onto an Au electrode surface via the formation of the Au-S bond significantly enhanced the catalytic properties of the Au electrode for HER.[46] Exfoliated two-dimensional nanosheets deposited on a glassy carbon electrode via a drop-casting method also exhibit high catalytic activity for HER.[47]

In the 2H phase of transition metal dichalcogenides MX_2, where M is the metal (*e.g.* Mo, W, Nb, Ta) and X= S, Se or Te, the transition metal atom is coordinated by 6 chalcogen atom in a trigonal prismatic arrangement and possesses semiconducting properties.[49, 50] On the other hand, in the 1T phase, the trantistion metal atom presents an octahedral chalcogen coordination which results in a material with metallic properties. Fig. 7 shows the unit cell of 2H and 1T MoS_2. Chemical exfoliation of tungsten sulfide was used to prepare strained 1T WS_2 nanosheets. WS_2 powder was first intercalated by lithium to form Li_xWS_2, and was then exfoliated through forced hydration. The 1T WS_2 electrodes show HER activity comparable to nanostructured MoS_2 whereas the bulk (2H) WS_2 exhibits poor catalytic activity.[31] The exchange current density of exfoliated 1T WS_2 is ~2 x 10^{-5} A cm^{-2} and the Tafel slope is 55 mV dec^{-1}.

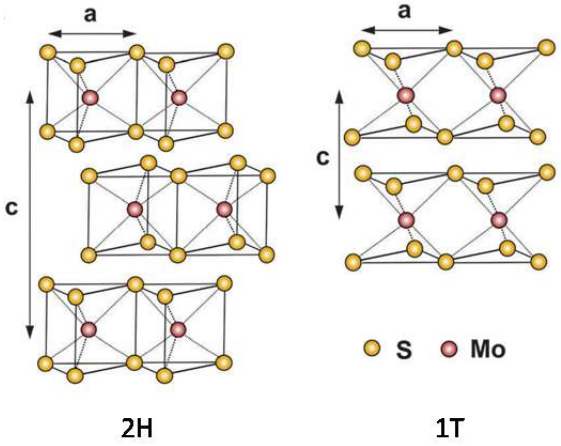

Fig. 7 Shcematic illustration of the 2H and 1T polymorphs of MoS_2. Reprinted with permission from ref. 49, copyright 2013, RSC Publishing.

A challenge encountered when using chemically exfoliated MoS_2 sheets is their tendency to restack during material processing, which hinders vertical charge transport and limits the access of protons to the catalytically active sites. Huang and co-workers reported the spontaneous decoration of Au nanoparticles on MoS_2 and WS_2 sheets upon direct reaction with a gold precursor ($HAuCl_4$) in water.[51] The presence of Au nanoparticles on the chemically exfoliated nanosheets greatly improves charge transport between the sheets and enhances their catalytic HER efficiency.

Jin and co-workers addressed the difficulty to obtain a high number of edge sites while keeping a good electric contact to the catalyst by growing exfoliated MoS_2 nanosheets directly on conductive substrates. They first prepared flowerlike MoS_2 nanoparticles with a high density of exposed edges directly on graphite via chemical vapour deposition (CVD). Then, the multilayered semiconducting MoS_2 was converted into the metallic 1T-MoS_2 polymorph by lithium intercalation and exfoliation as previously described for WS_2. This electrode achieved a current density of 10 mA cm^{-2} at η = 187 mV and a Tafel slope of 43 mV dec^{-1}.[52]

Cui and co-workers recently reported the continuous tuning of vertically aligned MoS_2 nanofilms through electrochemical

intercalation of Li^+ ions.[53] Intercalation of Li at different voltages vs. Li^+/Li in nanofilms with molecular layers perpendicular to the substrates allows the tuning of the layer spacing, Mo oxidation state, and the ratio of semiconducting 2H to metallic 1T phase of MoS_2 (Fig. 8a). The pristine MoS_2 exhibits an exchange current density j_0 = 3.4x10^{-6} A cm^{-2} and Tafel slope of 123 mV dec^{-1}. The Tafel slope can be reduced to 60 mV dec^{-1} by electrochemical Li intercalation and discharge at 1.5 V vs. Li^+/Li. The HER catalytic activity of the MoS_2 nanofilms is further improved by Li electrochemical intercalation at 1.2 and 1.1 V due to a phase transition from the 2H to 1T phase. The Tafel slope decreases to 44 mV dec^{-1} (Fig. 8b), in agreement with that of the chemically exfoliated 1T MoS_2[52] and 1T WS_2[31] nanosheets.

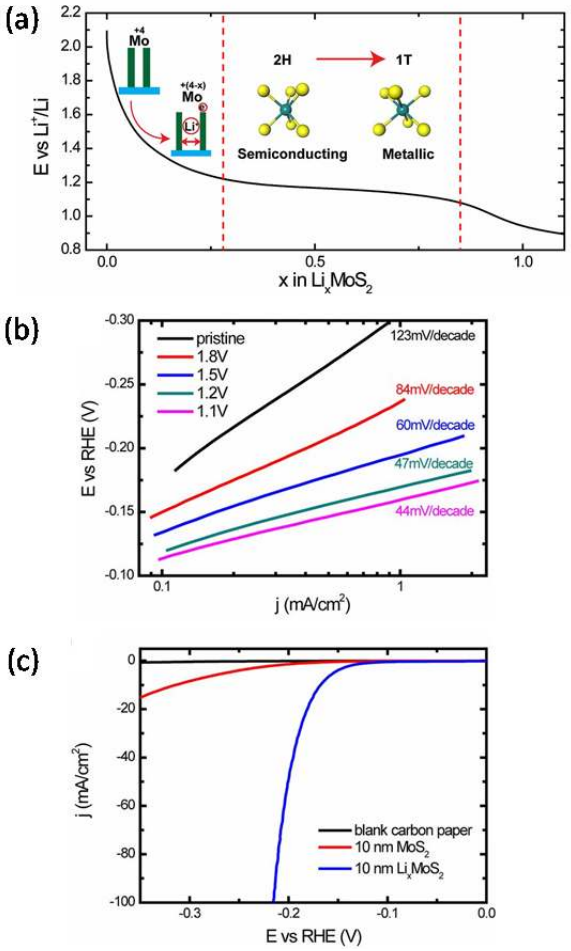

Fig. 8 (a) Galvanostatic discharge curve representing the lithiation process. Li intercalates into the van der Waals gaps of MoS_2 to donate electrons to the slabs and expand the layer spacing. The voltage monotonically drops to 1.2 V vs. Li^+/Li to reach a Li content of 0.28, after which the system undergoes a 2H to 1T MoS_2 first-order phase transition. The atomic structure is changed from trigonal prismatic to octahedral, along with the change from semiconducting to metallic. (b) Tafel slope of MoS_2 is continuously tuned by Li electrochemical intercalation at different voltages. The slope reaches 44 mV dec^{-1} at 1.1 V vs. Li^+/Li. (c). HER activity of MoS_2 is enhanced by Li intercalation. The Tafel slope is reduced from 123 mV dec^{-1} (pristine MoS_2) to 44 mV dec^{-1} (lithiated MoS_2). Reprinted with permission from ref. 53, copyright 2013, PNAS.

Atomic layer deposition (ALD) of 10 nm MoO_3 on a 3D carbon fiber paper (CFP) followed by a rapid sulfurization process produced a high-surface-area MoS_2 electrode. The as prepared electrode has Tafel slope of 98 mV dec^{-1}. The nanostructured electrode obtained after electrochemical Li intercalation and discharging at 0.7 V vs. Li^+/Li of this high-surface-area electrode requires only 168 and 216 mV overpotential to drive 10 and 100 mA cm^{-2} of HER current density, respectively (Fig. 8c).

2.2 Molybdenum carbides

Metal carbides have been studied for their platinum-like properties. The inclusion of carbon into the metal lattices broadens the metal d-band structure which resembles that of Pt.[54, 55] Furthermore, a correlation between the downshift of the d-band center and the decrease of the hydrogen binding energy (HBE) was established.[56] These properties are of particular interest for hydrogenation reactions, including HDT and HER. Oyama and co-workers pioneered the use of Mo_2C as HDT catalyst in 1988.[57] They showed that Mo_2C has good activity for HDN,[57] moderate activity for HDS, and limited activity for HDO.[58, 59] However, studies of Mo_2C as a potential HER catalyst are only recent.

Chen and co-workers investigated the electrochemical stability of Mo_2C, WC, and W_2C in aqueous solutions at different pHs in 2012.[60] Hydrogen evolution was observed at cathodic potentials for Mo_2C-modified electrodes. A current density of 0.1 mA cm^{-2} was attained at η = 150 mV at pH = 0.5.[60] Whether this current density is solely due to HER or it includes capacitive charging current was not probed. Likewise, the HER property of Mo_2C was not investigated in detail. Schröder and co-workers surveyed the same year different transition metal carbides, nitrides, sulphides, and borides for HER. They found that to reach 20 mA cm^{-2}, Mo_2C needs η = 600 mV. Thus, the activity of Mo_2C is at most modest. It should be noted that the measurements were done on bulk materials with small BET surface areas.[61] A first thorough investigation of the HER activity of Mo_2C was reported by our group. We found that commercial Mo_2C micro particles (Fig. 9a) are highly active and stable catalysts for HER in both acidic and alkaline solutions (Fig 9b).[62] The overpotential to reach 10 mA cm^{-2} is 200 mV in acid and 190 mV in base. The Tafel slope is about 55 mV dec^{-1}.[62] The discrepancy of the activity of Mo_2C reported in these two studies (one by us and the other one by Schröder) is surprising and might be due to different sources of Mo_2C, or different methods of electrode preparation, or both.

As discussed in section 2.1, the electrocatalytic activity of a given material might be improved if the density of exposed active sites in the material is increased. Reducing the particle size of catalyst to the nanometer scale is an efficient approach in this context. A second approach is to use porous and conductive support such as carbon nanotubes to improve the conductivity of the catalytic system and to favour the dispersion of catalyst. Decreasing the d-band center of Mo_2C is an

additional method to enhance its catalytic activity. These approaches have been pursued to improve the HER activity of Mo_2C.

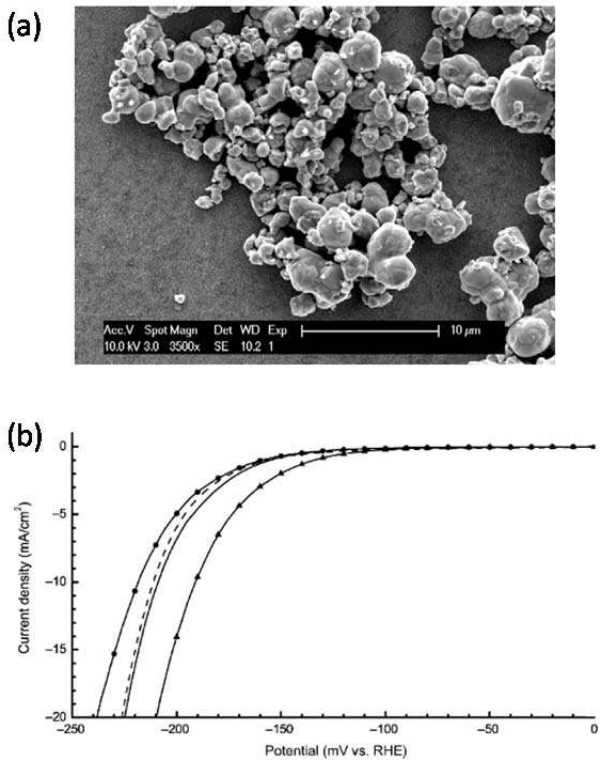

Fig. 9 (a) SEM image of Mo_2C microparticles. (b) HER polarization curves (10^{th}) of MoB and Mo_2C at pH 0 and 14. Scan rate=1 mV s^{-1}. MoB, pH 0, 2.5 mg cm^{-2} (- - - -); MoB, pH 14, 2.3 mg cm^{-2} (—•—); Mo_2C, pH 0, 1.4 mg cm^{-2} (—); Mo_2C, pH 14, 0.8 mg cm^{-2} (— ▲ —). The iR drop was corrected. Reprinted with permission from ref. 62, copyright 2012, Wiley-VCH.

Using carbon black and carbon nanotubes (CNT) as support, Chen *et al.* prepared Mo_2C nanoparticles with an average size of 12 nm.[63] The particles were synthesized by the carburization of carbon-supported ammonium molybdate. The particles are well dispersed with no aggregation, resulting in a high density of available active sites, and improved electronic conductivity. The authors also proposed that the anchoring of Mo_2C on the carbon support downshifts the d-band center of molybdenum which decreases the hydrogen binding energy.[63] Consequently, the Mo_2C particles supported on CNT (Mo_2C/CNT) reach current density of 10 mA cm^{-2} at η = 152 mV. The Tafel slope is 55 mV dec^{-1} and the exchange current density is $1.4x10^{-5}$ A cm^{-2} in 0.1 M $HClO_4$.[63] This activity is much higher than a bulk Mo_2C used as a reference in the same study, and is considerably higher than the Mo_2C microparticles used in our earlier study. The long term stability of the Mo_2C/CNT catalyst was confirmed by 3000 cycles of potential sweeps.

The porosity of the nanocatalyst itself has been reported to enhance HER catalysis by Liu, Tang, and co-workers.[64] Nanoporous Mo_2C nanowires were synthesized by pyrolysis of a MoO_x/amine hybrid precursor under an inert atmosphere. The high aspect ratio nanowires are several micrometers in length and 80-150 nm in width (Fig. 10a). HRTEM shows these nanowires are composed of discrete nanoparticles of 10-15 nm (Fig. 10b). The catalyst exhibits excellent HER activity. In 0.5 M H_2SO_4, the current j = 10 mA cm^{-2} at η = 130 mV, and j = 60 mA cm^{-2} at η = 200 mV are reached with a Tafel slope of 53 mV dec^{-1} (Fig. 10c). This superior activity of np-Mo_2C NWs was attributed to their large surface areas, nanosized crystallites and nanoporosity. The large surface area and small crystallite size bring about a higher number of exposed active sites. The porosity also prevents the aggregation of the catalyst. The stability of the catalyst was also confirmed in a 1000-cycle potential cycling experiment. For comparison, the catalytic activity of both commercial and synthetic Mo_2C microparticles was measured. At η = 200 mV, j is below 10 mA cm^{-2} for the Mo_2C microparticles.

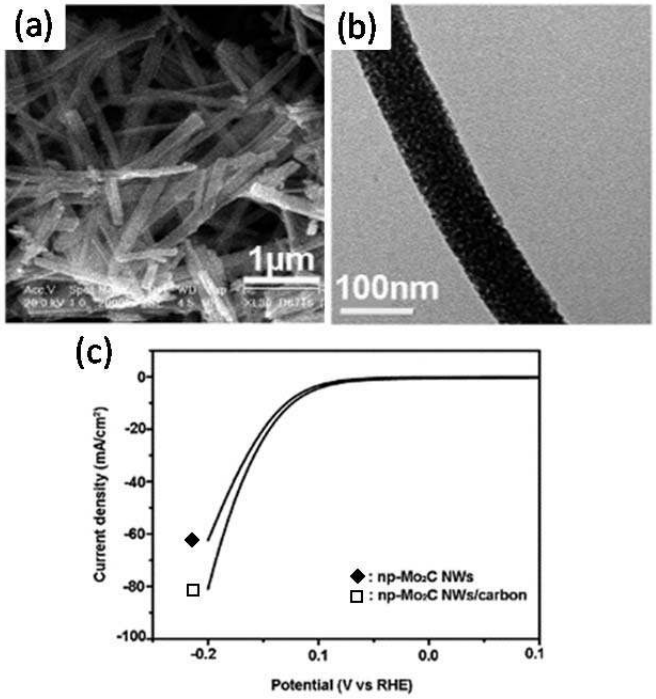

Fig. 10 (a) SEM picture of Mo_2C nanowires. (b) TEM picture of a nanowire revealing assemblies of smaller discrete Mo_2C nanoparticles. (c) HER polarization curves of the material itself (◆) and of the carbon supported catalyst (□) in 0.5 M H_2SO_4 with loadings of 210 μg cm^{-2}. Reprinted with permission from ref. 64, copyright 2013, RSC Publishing.

The catalytic activity of np-Mo_2C NWs was further enhanced by mixing the nanowires with commercial Vulcan carbon.[64] This hybridization provided an even higher dispersion of catalyst and also improved electron transfer. Consequently, j is increased to 80 mA cm^{-2} from 60 mA cm^{-2} at η = 200 mV (Fig. 10c) and the Tafel slope is 54 mV dec^{-1}.

Chen *et al.* sought to combine Mo_2N with Mo_2C. They achieved this using soybean as the carbon and nitrogen source and ammonium molybdate as the molybdenum source in a solid state reaction.[65] The optimal molybdate to soybean ratio was one to one (Mo_1Soy). It was found that within Mo_1Soy Mo_2N and Mo_2C co-existed with a grain size of 1.7 nm and 9.4 nm, respectively. As Mo_2C/C nanoparticles (8.5 nm in grain size) have similar onset overpotential as Mo_1Soy in HER, the Mo_2C phase of Mo_1Soy was the main catalyst. Nevertheless, Mo_1Soy has higher global HER activity than carbon-supported Mo_2N (Mo_2N/C) or carbon-supported Mo_2C (Mo_2C/C) alone.[65] For Mo_1Soy, j = 10 mA cm^{-2} at η = 180 mV.[65] For Mo_2C/C and Mo_2N/C, j = 10 mA cm^{-2} at η = 220 mV and 300 mV, respectively.[65] Interestingly, a physical mixture of Mo_2C/C and Mo_2N/C was not as active as Mo_1Soy. Thus, the high activity of Mo_1Soy results from a synergism between the two molybdenum phases in the hybrid material. The same group then applied reduced graphene oxide (RGO) sheets as support to further enhance the activity of Mo_1Soy. The resulting catalyst (Mo_1Soy-RGO) consists of nanoparticles of Mo_2N and Mo_2C (1 to 7 nm in size) uniformly dispersed on RGO sheets. The HER activity was improved: j = 10 mA cm^{-2} at η = 110 mV (Fig. 11a and 11b).[65]

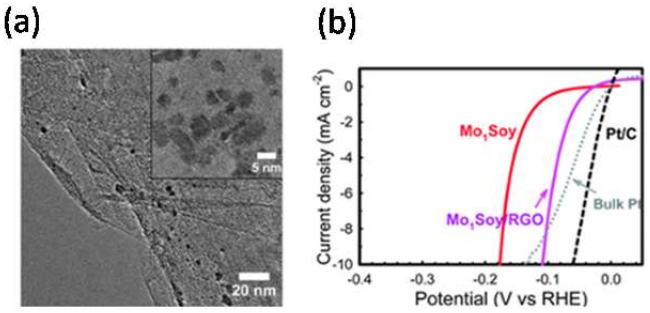

Fig. 11 (a) RGO-supported Mo_1Soy catalyst. The inset picture is a HRTEM image with a magnification of 500'000. (b) The HER polarization curve of RGO-supported Mo_1Soy catalyst (loading of Mo_2C: 0.47 mg cm^{-2}) demonstrating the enhancement by RGO. Reprinted with permission from ref. 67, copyright 2013, RSC Publishing.

The improvement brought by the RGO support might be attributed to a higher conductivity of the system and the coupling of RGO with catalyst. The stability of Mo_1Soy, Mo_1Soy-RGO, Mo_2N/C and Mo_2C/C was tested in 3000 potential sweeps. For Mo_1Soy and Mo_1Soy-RGO, the activity was similar before and after 3000 potential sweeps; the overpotentials increased only 7 mV.[65] However, for Mo_2C/C, the overpotential increased 100 mV after the test. These results pointed to a synergistic effect between Mo_2N and Mo_2C that also improved the stability of catalyst.

2.3 Promoted molybdenum nitrides (Mo_xN)

Molybdenum nitrides were extensively studied for HDT reactions,[57, 59] however, they were only recently studied for HER, mostly in combination with a promoting metal.

Chen *et al.* applied nickel to improve molybdenum nitride in HER catalysis. Molybdenum binds H strongly, while nickel binds it weakly. The $NiMoN_x$ material was designed to benefit from the compromise of both properties, resulting in modest hydrogen adsorption energy. They prepared carbon-supported nickel-molybdenum nitride nanosheets ($NiMoN_x$/C).[66] First, carbon-supported $(NH_4)_6Mo_7O_{24}$ and $Ni(NO_3)_2$ precursors were reduced to NiMo metal particles by H_2 at 400°C. The NiMo particles were then reacted with NH_3 at 800°C to give $NiMoN_x$/C nanosheets. The atomic ratio of Ni:Mo was 1:4.7 according to energy dispersive X-ray spectroscopy (EDX). The thickness of the nanosheets ranged from 4 to 15 nm; the average stacking number of the sheets is six. The main part of nanosheets was exfoliated and present in the form of single sheet. Compared with NiMo nanoparticles, $NiMoN_x$/C exhibited a higher stability and corrosion resistance in acidic media, demonstrated by a lower current density at highly positive potentials. In terms of HER, the following results were obtained for $NiMoN_x$/C in 0.1 M $HClO_4$: j = 5 mA cm^{-2} at η = 225 mV; the Tafel slope was 36 mV dec^{-1}. On the contrary, the following results were obtained for MoN/C: j = 5 mA cm^{-2} at η = 360 mV; the Tafel slope was 54.5 mV dec^{-1}. X-ray absorption spectroscopy (XAS) showed that Mo in $NiMoN_x$/C had a higher occupation of the d band than that of Mo in MoN. XAS also showed the Ni-Ni distance increased and Ni-Mo distance decreased upon incorporation of N. These geometric changes lowered the d-band center which resulted in a lower hydrogen bonding energy. Therefore, $NiMoN_x$/C was a better HER catalyst than NiMo.

Along the same line, Cao *et al.* used Co to modify the HER activity of Mo_xN. They prepared a ternary cobalt molybdenum nitride of the formula $Co_{0.6}Mo_{1.4}N_2$; this compound has a four-layered stacking sequence of a mixed close packed structure with alternating layers of transition metals in octahedral and trigonal prismatic coordination.[67] The primary particles of $Co_{0.6}Mo_{1.4}N_2$ are about 80 nm in size and have no well-defined facets; these primary particles aggregate to form large microparticles of several microns. The catalyst exhibits good HER activity: j = 10 mA cm^{-2} at η = 200 mV in 0.1 M $HClO_4$ (after correction of resistance of 25 Ω). In alkaline conditions, the catalyst requires 100 mV more of overpotential to reach the same current density as in the acid. It was proposed that Co promotes the catalyst activity as it affects the d-band structure of the Mo metal.[67]

2.4 Tungsten carbides (W_xC) and tungsten carbonitride (WCN) composites

The "platinum-like" catalytic behavior of tungsten carbides was established by Boudart and Levy in 1973.[55] This character of tungsten carbides is relevant to hydrogenation reactions. Consequently, tungsten carbides have been explored for HDT reactions,[58, 59] and for HER.[68-74] For example, Sokolsky *et al.*

reported j = 1 mA cm^{-2} at η = 300 mV and a Tafel slope of about 120 mV dec^{-1} at high η for WC in 1975.[68] Recently, Schröder and co-workers showed that bulk WC had j = 10 mA cm^{-2} at η = 300 mV.[61] W_2C has also been tested for HER.[71, 74, 75] Ham *et al.* reported that W_2C microparticles gave j = 23 mA cm^{-2} at η = 200 mV with a Tafel slope of 120 mV dec^{-1} in 2008.[74] Motivated by these promising results and the intrinsic properties of WC, further investigations of the HER activity of tungsten carbides were performed to improve their activity. Nanostructuring was the strategy chosen by several groups.

Burstein and co-workers compared the HER activity of WC particles prepared by microwave carburisation and by furnace heating.[76] The microwave synthesis produced particles with a finer grain size which were better catalysts. The best catalyst was synthesized from WO_3 and C microwaved for 8 min at 1313 K. The resulting nanoparticles have a phase composition of 42% WC, 24% W_2C, and 34% WO_3; the particles size is 50 to 100 nm. This catalyst gave j = 10 mA cm^{-2} at η = 100 mV and a Tafel slope of 95 mV dec^{-1} in 1.5 M H_2SO_4.[76]

Further control in the catalyst size and phase composition was achieved by Takanabe and co-workers. They used mesoporous graphitic C_3N_4 (mpg-C_3N_4) as a reactive template to prepare tungsten carbide nanocrystals (5 nm).[77] The ordered pores of mpg-C_3N_4 provided a nanosized confinement for the syntheses, allowing the formation of nanomaterials with a uniform size. Systematic variation of precursor compositions and temperatures led to different compositions and structures for the final nanocarbides (W_2C or WC). Both WC and W_2C exhibited high HER activity in 0.5 M H_2SO_4, but the best catalyst was the WC-1223 sample which contained mostly WC but also W_2C.[77] This catalyst exhibited j = 10 mA cm^{-2} at η = 125 mV and a Tafel slope of 84 mV dec^{-1}. The activity of WC-1223 was tested at different pHs; it was higher in more acidic media. The stability of the catalyst was confirmed by 800 polarization cycles.

The catalytic activity of metal carbides can be further modified by incorporation of nitrogen, as described earlier for Mo_2C. Nitridation of metal carbides is commonly done by direct ammonification at high temperatures. However, this method tends to give poor crystal growth and incomplete ammonification. The resulting metal carbonitrides have a low surface area and a low density of active sites. Zhao *et al.* developed a novel synthetic approach to prepare Fe-doped tungsten carbonitride (Fig. 10a).[78] Polydiaminopyridine (PDAP) was first synthesized from the nitrogen-rich monomer diaminopyridine in the presence of Na_2WO_4. The protons released during the PDAP polymerization process reacted with Na_2WO_4 to give a hybrid nanomaterial which was composed of PDAP and H_2WO_4 nanoparticles. This hybrid nanomaterial was pyrolyzed in the presence of iron to form a N-rich tungsten carbonitride material (Fe-WCN). The Fe-WCN exhibits several desirable features: (1) it consists of uniform and small nanoparticles (10-20 nm); (2) it has a nitrogen-rich backbone; (3) it has a pure tungsten carbonitride crystal structure. The optimal pyrolysis temperature was 800^{o}C. At pH = 1, Fe-WCN gave a j = 10 mA cm^{-2} at η = 220 mV, which is significantly higher than WCN. The latter was prepared by pyrolysis in the absence of Fe. The higher activity of Fe-WCN was attributed to higher conductivity and active surface, as Fe-WCN has an electrical resistance of 0.5 Ω cm and a BET area of 127.2 m^2 g^{-1} while WCN has a resistance of 2.6 Ω cm and a BET area of 79.2 m^2 g^{-1}.[78] The stability of Fe-WCN was confirmed by 3000 potential sweeps. At pH = 13, Fe-WCN gave j = 10 mA cm^{-2} at η = 250 mV. The high activity of Fe-WCN was also attributed to the presence of N-bound W species. The inclusion of nitrogen was suggested to downshift the d-band center of WC, since the W atoms in WN are more electropositive than W atoms in WC due to the higher electronegativity of N compared with C.[78] This leads to a weaker M-H binding energy and faster HER.

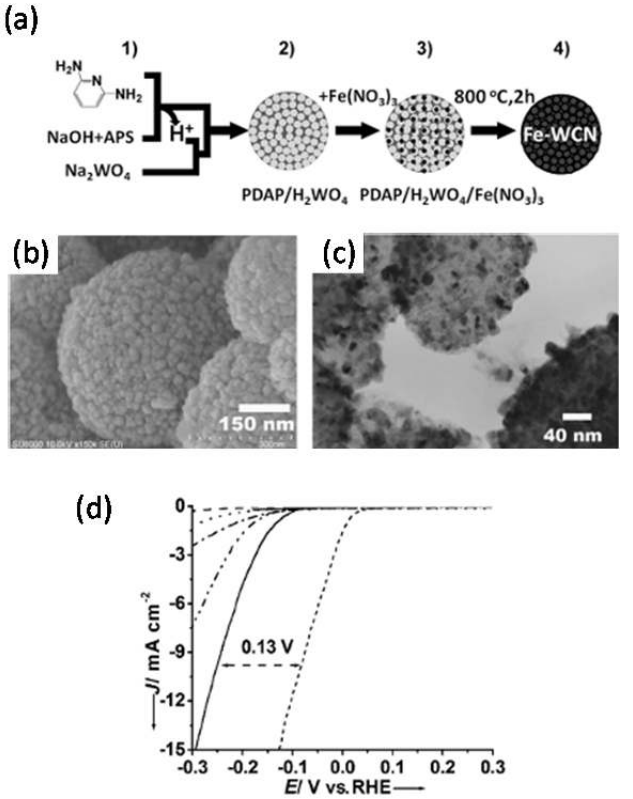

Fig. 12 (a) Synthesis of Fe-WCN materials. (b) SEM and (c) TEM micrographs of the electrocatalyst Fe-WCN-800. (d) HER polarization curves of glassy carbon (– – –), CN-800 (••••), FeCN (•–•–), WCN-800 (–••–••), Fe-WCN-800 (—), and commercial Pt/C (- - - -) catalyst in a pH 1 H_2SO_4 electrolyte (catalyst loading is 400 μg cm^{-2}). Reprinted with permission from ref. 78, copyright 2014, Wiley-VCH.

2.5 Nickel phosphide (Ni_2P)

Ni_2P has been thoroughly studied as a catalyst for HDT especially for HDS.[79, 80] An extended review on the HDT activity of transition metal phosphides including Ni_2P is available in the literature and interested readers are referred to it.[80] The activity of Ni_2P is the highest among all transition

metal phosphides. This high activity was subjected to extended experimental and theoretical investigations.

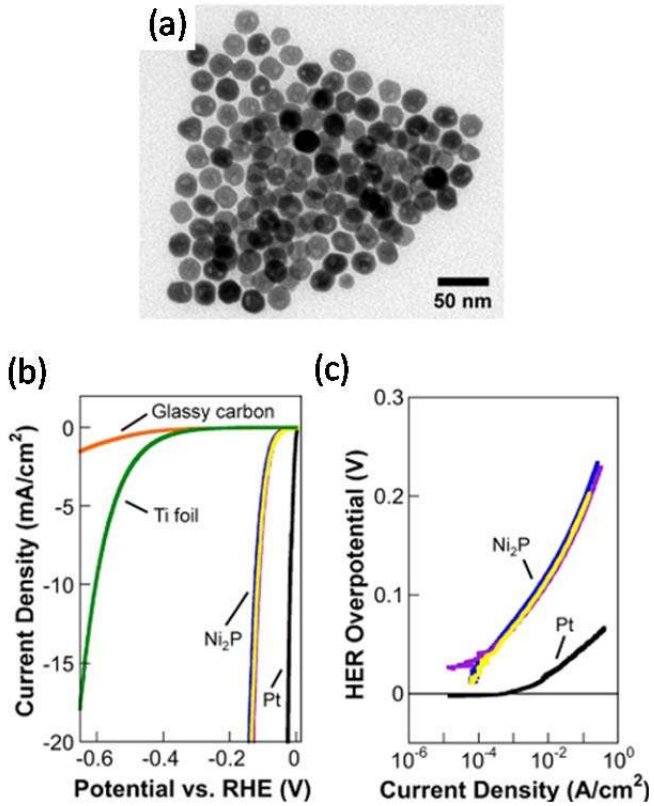

Fig. 13 (a) TEM image of Ni_2P nanoparticles. (b) Polarization data for three individual Ni_2P electrodes (loading 1 mg cm^{-2}) in 0.5 M H_2SO_4, along with glassy carbon, Ti foil, and Pt in 0.5 M H_2SO_4, for comparison. (c) Corresponding Tafel plots for the Ni_2P and Pt electrodes. Reprinted with permission from ref. 20, copyright 2013, American Chemical Society.

Continued from their previous theoretical studies of Ni_2P-catalyzed HDS reactions,[81] Rodriguez and co-workers examined the HER activity of Ni_2P by DFT calculations.[19] According to the calculations, the (001) face of Ni_2P has a modest hydrogen absorption energy and should be a good HER catalyst. Notably, they predicted that an ensemble effect favours HER by reducing the number of Ni active sites, thereby decreasing the energy cost for hydrogen removal from Ni_2P. Recently, Popczun *et al.* reported that nanostructured nickel phosphides are indeed an active electrocatalyst for HER in acidic solutions.[20] They synthesized uniformly distributed and multifaceted nanoparticles of Ni_2P which have an average grain size of 17 nm (Fig. 13a). When deposited on Ti, the Ni_2P nanoparticles showed a high activity in 0.5 M H_2SO_4: j = 10 mA cm^{-2} at η = 115 mV (Fig. 13b). The nanostructuring allowed the exposure of numerous active sites on the desired facet (001) where the ensemble effect could take place. Interestingly, the Tafel slopes changed at different overpotentials: it is 46 mV dec^{-1} between 25 mV to 125 mV, and 81 mV dec^{-1} between 150 mV and 200 mV (Fig. 13c). There was a small degradation of catalytic activity. After 500 potential sweeps, the overpotential required to reach 10 mA cm^{-2} rose from 115 mV to 140 mV.[20] However, this might be associated with the stability of the Ti-Ni_2P assembly rather than the stability of Ni_2P itself.

2.6 Miscellaneous

A few other materials have been investigated for both HDT and HER reactions. FeP has been tested for HDO[79] and HER. Motivated by the enhancement of catalytic activity brought by nanostructuring, Zhang and co-workers synthesized nanoporous FeP nanosheets by reaction of an inorganic–organic hybrid $Fe_{18}S_{25}$–TETAH (TETAH = protonated triethylenetetramine) nanosheets with trioctylphosphine at an elevated temperature.[82] The synthetic route resulted in FeP nanosheets having a porous structure, with a particle size of about 10 nm. These particles gave j = 10 mA cm^{-2} at η = 250 mV, with a Tafel slope of 67 mV dec^{-1} at pH = 0.

The activity of iron sulphide as a HDS catalyst was reported by Raje and Dadyburjor.[83] Recently, Di Giovanni *et al.* studied FeS nanoparticles as a HER catalyst. The nanoparticles are prepared under solvothermal conditions using $Fe_2S_2(CO)_6$. TEM pictures showed hexagonally shaped particles with crystallite sizes of 50 to 500 nm. The catalytic activity of the material was tested in 0.1 M potassium phosphate buffer (pH 7). The activity was modest: j = 0.05 mA cm^{-2} at η = 450 mV.[84] NbC was studied for HDT and its activity was improved by Oyama and co-workers.[58, 85, 86] Schröder and co-workers found that commercial NbC particles (ca. 500 nm) exhibited rather low activity for HER: j = 20 mA cm^{-2} at η = 739 mV at pH = 1.[54, 61]

3 Conclusions

In summary, recent developments of electrocatalysts of HER have profited from the knowledge acquired in the study of hydrotreating catalysts and the understanding of reactivity trends on transition metal surfaces. HDT and HER catalysts rely on the exposure of specific sites capable of adsorbing and desorbing hydrogen with low energetic barriers. In this review, we have highlighted a number of HDT catalysts that are also active for HER. Moreover, we have presented different nanostructuring approaches to improve the activity of electrocatalysts. Table 1 summarizes some of the start-of-the-art materials.

MoS_2 nanosheets with a high ratio of edge to basal sites grown on a conductive graphene scaffold are capable of driving 10 mA cm^{-2} at η = 140 mV. MoS_2 nanofilms prepared by Li intercalation can achieve j = 100 mA cm^{-2} at η = 220 mV.[53] Other HDT catalysts have also shown high activity. State-of-the-art Mo_2C can drive 10 and 80 mA cm^{-2} at overpotentials of 125 and 200 mV, respectively.[64] Moreover, these catalysts are active and stable in both basic and acidic media.

Nanostructured Ni_2P can deliver 20 and 100 mA cm^{-2} at η = 130 and 180 mV, respectively.[20]

The challenge of producing hydrogen at a scale comparable to our energy demands is great and the response of the scientific community has been swift. Computational tools have been effectively applied on the development of HER electrocatalysts. Improved understanding of catalysis has allowed us to move away from a traditional trial-and-error approach to purposely construct nanostructured materials. Impressive advances have been made in the last years and this trend is expected to continue. A repertoire of non-precious and highly active HER catalysts will be available in the near future. Although none of such catalysts might outperform Pt in terms of activity, they are valid Pt replacements when cost and availability are taken into account.

4 Outlook

Looking ahead, many challenges in the development of HER catalysts remain. While all catalysts cited here are made of earth-abundant elements, they are not necessary cheap to make as sophisticated and costly procedures are often involved. Likewise, nanostructuring is mostly limited to the preparation of a small amount of material in a laboratory scale. Scale-up of synthetic methods needs to be addressed before considering realistic application. In parallel to this, a HER catalyst should be evaluated according to the target application. The production of hydrogen in an electrolyzer requires a catalyst to deliver current densities in the order of 1000 mA cm^{-2}; on the other hand, hydrogen production from a photoelectrochemical (PEC) cell requires a catalyst to deliver a current density of only 10 mA cm^{-2}. The latter application is the most cited driver for the current development in HER electrocatalysts. The integration of electrocatalysis into photoelectrochemical (PEC) cells is not straightforward. In this sense, a number of new challenges become evident, and two of them are listed here.

(1) Additional stability issues. In PEC applications, the electrocatalyst has to be stable under illumination (reductive) conditions, but it need also to be stable in the dark where the open cell potential of the photoelectrode could become very oxidative and, thus, oxidative corrosion is a major decomposition pathway.

(2) The catalyst should not absorb or refract light in the visible range and should have an adequate electric contact with the underlying photoabsorbing semiconductor. Many of the nanostructuring strategies summarized here are not easily adapted to the preparation of PEC water splitting devices. Conductive substrates such as graphene have high light absorption coefficients; thick HER catalysts block a great part of the incident light. Both are detrimental to photoelectrocatalysis. Processing at a high temperature could damage the photo absorber material inducing changes in morphology, reducing the density of charge carriers, or creating trap and recombination sites on the surface of the photoelectrode. Physical adsorption of catalysts by drop-casting or self-assembly is a simple and potentially scalable method for the deposition of catalyst on photoelectrodes. However, the injection of excited electrons into the HER catalysts can be hindered if a proper electronic contact is not created between the photoabsorber and the electrocatalyst.

Orthogonalization of light absorbance and fuel production in high-aspect ratio photoelectrodes is an attractive approach in direct solar water splitting. In this context, electrodeposition, photoelectrodeposition and methods such as ALD and CVD that allow the conformal coating of the photoelectrode with an electrocatalyst are attractive methods for the preparation of HER catalysts. .

Table 1 Summary of some state-of-the-art HER electrocatalysts.

Material	Morphology	Particles size	η_{10} [mV]	Tafel Slope [mV dec^{-1}]	Exchange current densities [10^{-6} A cm^{-2}]	Conditions (electrolyte, loading)	Ref.
MoS_2	Nanoparticles on reduced graphene	N/A	140	41	5.1	0.5 M H_2SO_4 285 μg cm^{-2}	43
MoS_2	Double-gyroid bicontinous network	N/A	220	50	0.69	0.5 M H_2SO_4 60 μg cm^{-2}	35
MoS_2	Vertically aligned MoS_2 nanofilms	N/A	168	44	N/A	0.5 M H_2SO_4 120 μg cm^{-2}	53
WS_2	Exfoliated 1T WS_2	N/A	210	55	20	0.5 M H_2SO_4 0.1-0.2 μg cm^{-2}	31
Mo_2C	Microparticles	1-3 μm	190	54	3.8	1 M KOH 800 μg cm^{-2}	62
Mo_2C	Nanoparticles	7-15 nm	152	55	14	0.1 M $HClO_4$ 2 mg cm^{-2}	63
Mo_2C	Carbon-supported porous nanowires made of discrete nanoparticles	10-15 nm	125	54	N/A	0.5 M H_2SO_4 210 μg cm^{-2}	64
$NiMoN_x$	Carbon-supported nanosheets	4-15 nm	N/A	36	240	0.1 M $HClO_4$ 250 μg cm^{-2}	66
$Co_{0.6}Mo_{1.4}N_2$	Nanocrystallites	80 nm	200	N/A	230	0.1 M $HClO_4$ 23 μg cm^{-2}	67
Mo_1Soy-RGO	Superimposed RGO sheets made of crystalline stripes	1-7 nm	109	63	37	0.1 M $HClO_4$ 470 μg cm^{-2}(Mo_2C)	65
W_2C	Microspheres	2-5 μm	190	118	281	1 M H_2SO_4 N/A	74
W_2C	Nanoparticles	16.5 nm	200	N/A	N/A	0.1 M H_2SO_4 263 mg cm^{-2}	75
WC	Nanocrystals	5.6 nm	125	84	350	0.5 M H_2SO_4 1 mg cm^{-2}	77
Fe-WCN	Spherical nanoparticles	10-20 nm	220	47	N/A	0.05 M H_2SO_4 400 μg cm^{-2}	78
Ni_2P	Hollow spherical nanoparticles	17 nm	115	46	33	0.5 M H_2SO_4 1 mg cm^{-2}	20
FeP	Nanosheets	10 nm	240	67	N/A	0.5 M H_2SO_4 280 μg cm^{-2}	82

Acknowledgements

This work is supported by a starting grant from the European Research Council under the European Community's Seventh Framework Programme (FP7 2007-2013)/ERC Grant agreement no. 257096.

Notes and references

[a] Laboratory of Inorganic Synthesis and Catalysis, Institute of Chemical Sciences and Engineering, École Polytechnique Fédérale de Lausanne (EPFL), EPFL-ISIC-LSCI, BCH 3305, Lausanne, CH 1015, Switzerland. E-mail: xile.hu@epfl.ch; Fax: +41 216939305; Tel: +41 216939781

1. J. O. M. Bockris, *Int. J. Hydrogen Energy*, 2002, **27**, 731-740.
2. Y. Tachibana, L. Vayssieres and J. R. Durrant, *Nat. Photonics*, 2012, **6**, 511-518.
3. G. A. Olah, *Angew. Chem. Int. Ed.*, 2013, **52**, 104-107.
4. J. R. Rostrup-Nielsen, *Catal. Rev. Sci. Eng.*, 2004, **46**, 247-270.
5. M. Gratzel, *Nature*, 2001, **414**, 338-344.

6. T. R. Cook, D. K. Dogutan, S. Y. Reece, Y. Surendranath, T. S. Teets and D. G. Nocera, *Chem. Rev.*, 2010, **110**, 6474-6502.
7. A. Paets van Troostwijk and J. R. Deiman, *Obs. Phys.*, 1789, **35**, 369.
8. R. de Levie, *J. Electroanal. Chem.*, 1999, **476**, 92-93.
9. D. Merki and X. Hu, *Energy Environ. Sci.*, 2011, **4**, 3878-3888.
10. A. B. Laursen, S. Kegnaes, S. Dahl and I. Chorkendorff, *Energy Environ. Sci.*, 2012, **5**, 5577-5591.
11. S. Trasatti, *Electrochim. Acta*, 1984, **29**, 1503-1512.
12. R. Parsons and J. O. M. Bockris, *J. Chem. Soc. Faraday Trans.*, 1951, **47**, 914-928.
13. S. Fletcher, *J. Solid State Electrochem.*, 2009, **13**, 537-549.
14. J. O. M. Bockris and E. C. Potter, *J. Electrochem. Soc.*, 1952, **99**, 169-186.
15. J. K. Nørskov, T. Bligaard, A. Logadottir, J. R. Kitchin, J. G. Chen, S. Pandelov and U. Stimming, *J. Electrochem. Soc.*, 2005, **152**, J23-J26.
16. B. Hinnemann, P. G. Moses, J. Bonde, K. P. Jørgensen, J. H. Nielsen, S. Horch, I. Chorkendorff and J. K. Nørskov, *J. Am. Chem. Soc.*, 2005, **127**, 5308-5309.
17. W. I. Choi, B. C. Wood, E. Schwegler and T. Ogitsu, *J. Phys. Chem. C*, 2013, **117**, 21772-21777.
18. J. Greeley, T. F. Jaramillo, J. Bonde, I. Chorkendorff and J. K. Nørskov, *Nat. Mater.*, 2006, **5**, 909-913.
19. P. Liu and J. A. Rodriguez, *J. Am. Chem. Soc.*, 2005, **127**, 14871-14878.
20. E. J. Popczun, J. R. McKone, C. G. Read, A. J. Biacchi, A. M. Wiltrout, N. S. Lewis and R. E. Schaak, *J. Am. Chem. Soc.*, 2013, **135**, 9267-9270.
21. H. Topsøe, B. Clausen and F. Massoth, in *Catalysis*, eds. J. Anderson and M. Boudart, Springer Berlin Heidelberg, 1996, vol. 11, pp. 1-269.
22. P. Liu, J. A. Rodriguez, T. Asakura, J. Gomes and K. Nakamura, *J. Phys. Chem. B*, 2005, **109**, 4575-4583.
23. F. Besenbacher, M. Brorson, B. S. Clausen, S. Helveg, B. Hinnemann, J. Kibsgaard, J. V. Lauritsen, P. G. Moses, J. K. Nørskov and H. Topsøe, *Catal. Today*, 2008, **130**, 86-96.
24. A. S. Walton, J. V. Lauritsen, H. Topsøe and F. Besenbacher, *J. Catal.*, 2013, **308**, 306-318.
25. A. K. Tuxen, H. G. Füchtbauer, B. Temel, B. Hinnemann, H. Topsøe, K. G. Knudsen, F. Besenbacher and J. V. Lauritsen, *J. Catal.*, 2012, **295**, 146-154.
26. L. P. Hansen, Q. M. Ramasse, C. Kisielowski, M. Brorson, E. Johnson, H. Topsøe and S. Helveg, *Angew. Chem. Int. Ed.*, 2011, **50**, 10153-10156.
27. M. Brorson, A. Carlsson and H. Topsøe, *Catal. Today*, 2007, **123**, 31-36.
28. M. Breysse, E. Furimsky, S. Kasztelan, M. Lacroix and G. Perot, *Catal. Rev. Sci. Eng.*, 2002, **44**, 651-735.
29. R. R. Chianelli, G. Berhault, P. Raybaud, S. Kasztelan, J. Hafner and H. Toulhoat, *Appl. Catal., A*, 2002, **227**, 83-96.
30. T. F. Jaramillo, K. P. Jørgensen, J. Bonde, J. H. Nielsen, S. Horch and I. Chorkendorff, *Science*, 2007, **317**, 100-102.
31. D. Voiry, H. Yamaguchi, J. W. Li, R. Silva, D. C. B. Alves, T. Fujita, M. W. Chen, T. Asefa, V. B. Shenoy, G. Eda and M. Chhowalla, *Nat. Mater.*, 2013, **12**, 850-855.
32. H. I. Karunadasa, E. Montalvo, Y. Sun, M. Majda, J. R. Long and C. J. Chang, *Science*, 2012, **335**, 698-702.
33. H. Tributsch and J. C. Bennett, *J. Electroanal. Chem*, 1977, **81**, 97-111.
34. Z. Chen, D. Cummins, B. N. Reinecke, E. Clark, M. K. Sunkara and T. F. Jaramillo, *Nano Lett.*, 2011, **11**, 4168-4175.
35. J. Kibsgaard, Z. B. Chen, B. N. Reinecke and T. F. Jaramillo, *Nat. Mater.*, 2012, **11**, 963-969.
36. D. Kong, H. Wang, J. J. Cha, M. Pasta, K. J. Koski, J. Yao and Y. Cui, *Nano Lett.*, 2013, **13**, 1341-1347.
37. D. Kong, J. Cha, H. Wang, H. R. Lee and Y. Cui, *Energy Environ. Sci.*, 2013.
38. H. Wang, D. Kong, P. Johanes, J. J. Cha, G. Zheng, K. Yan, N. Liu and Y. Cui, *Nano Lett.*, 2013, **13**, 3426-3433.
39. Z. Wu, B. Fang, Z. Wang, C. Wang, Z. Liu, F. Liu, W. Wang, A. Alfantazi, D. Wang and D. P. Wilkinson, *ACS catal.*, 2013, **3**, 2101-2107.
40. J. Xie, H. Zhang, S. Li, R. Wang, X. Sun, M. Zhou, J. Zhou, X. W. Lou and Y. Xie, *Adv. Mater.*, 2013, **25**, 5807-5813.
41. J. Xie, J. Zhang, S. Li, F. Grote, X. Zhang, H. Zhang, R. Wang, Y. Lei, B. Pan and Y. Xie, *J. Am. Chem. Soc.*, 2013.
42. H. Vrubel, T. Moehl, M. Gratzel and X. Hu, *Chem. Commun.*, 2013, **49**, 8985-8987.
43. Y. Li, H. Wang, L. Xie, Y. Liang, G. Hong and H. Dai, *J. Am. Chem. Soc.*, 2011, **133**, 7296-7299.
44. Y. Yan, X. Ge, Z. Liu, J.-Y. Wang, J.-M. Lee and X. Wang, *Nanoscale*, 2013, **5**, 7768-7771.
45. J. Yang, D. Voiry, S. J. Ahn, D. Kang, A. Y. Kim, M. Chhowalla and H. S. Shin, *Angew. Chem. Int. Ed.*, 2013, n/a-n/a.
46. T. Wang, L. Liu, Z. Zhu, P. Papakonstantinou, J. Hu, H. Liu and M. Li, *Energy Environ. Sci.*, 2013, **6**, 625-633.
47. S. Ji, Z. Yang, C. Zhang, Z. Liu, W. W. Tjiu, I. Y. Phang, Z. Zhang, J. Pan and T. Liu, *Electrochim. Acta*, 2013, **109**, 269-275.
48. J. N. Coleman, M. Lotya, A. O'Neill, S. D. Bergin, P. J. King, U. Khan, K. Young, A. Gaucher, S. De, R. J. Smith, I. V. Shvets, S. K. Arora, G. Stanton, H.-Y. Kim, K. Lee, G. T. Kim, G. S. Duesberg, T. Hallam, J. J. Boland, J. J. Wang, J. F. Donegan, J. C. Grunlan, G. Moriarty, A. Shmeliov, R. J. Nicholls, J. M. Perkins, E. M. Grieveson, K. Theuwissen, D. W. McComb, P. D. Nellist and V. Nicolosi, *Science*, 2011, **331**, 568-571.
49. X. Huang, Z. Zeng and H. Zhang, *Chem. Soc. Rev.*, 2013, **42**, 1934-1946.
50. M. Chhowalla, H. S. Shin, G. Eda, L. J. Li, K. P. Loh and H. Zhang, *Nat. Chem.*, 2013, **5**, 263-275.
51. J. Kim, S. Byun, A. J. Smith, J. Yu and J. Huang, *J. Phys. Chem. Lett.*, 2013, **4**, 1227-1232.
52. M. A. Lukowski, A. S. Daniel, F. Meng, A. Forticaux, L. Li and S. Jin, *J. Am. Chem. Soc.*, 2013, **135**, 10274-10277.
53. H. Wang, Z. Lu, S. Xu, D. Kong, J. J. Cha, G. Zheng, P.-C. Hsu, K. Yan, D. Bradshaw, F. B. Prinz and Y. Cui, *Proc. Natl. Acad. Sci. USA*, 2013.
54. W.-F. Chen, J. T. Muckerman and E. Fujita, *Chem. Commun.*, 2013, **49**, 8896-8909.
55. R. B. Levy and M. Boudart, *Science*, 1973, **181**, 547-549.
56. J. K. Nørskov, F. Abild-Pedersen, F. Studt and T. Bligaard, *Proc. Natl. Acad. Sci. USA*, 2011, **108**, 937-943.

57. J. C. Schlatter, S. T. Oyama, J. E. Metcalfe and J. M. Lambert, *Ind. Eng. Chem. Res.*, 1988, **27**, 1648-1653.
58. S. Ramanathan and S. T. Oyama, *J. Phys. Chem.*, 1995, **99**, 16365-16372.
59. E. Furimsky, *Appl. Catal., A*, 2003, **240**, 1-28.
60. M. C. Weidman, D. V. Esposito, Y.-C. Hsu and J. G. Chen, *J. Power Sources*, 2012, **202**, 11-17.
61. S. Wirth, F. Harnisch, M. Weinmann and U. Schröder, *Appl. Catal., B*, 2012, **126**, 225-230.
62. H. Vrubel and X. Hu, *Angew. Chem. Int. Ed.*, 2012, **51**, 12703-12706.
63. W. F. Chen, C. H. Wang, K. Sasaki, N. Marinkovic, W. Xu, J. T. Muckerman, Y. Zhu and R. R. Adzic, *Energy Environ. Sci.*, 2013, **6**.
64. L. Liao, S. Wang, J. Xiao, X. Bian, Y. Zhang, M. D. Scanlon, X. Hu, Y. Tang, H. H. Girault and B. Liu, *Energy Environ. Sci.*, 2013.
65. W.-F. Chen, S. Iyer, S. Iyer, K. Sasaki, C.-H. Wang, Y. Zhu, J. T. Muckerman and E. Fujita, *Energy Environ. Sci.*, 2013, **6**, 1818-1826.
66. W.-F. Chen, K. Sasaki, C. Ma, A. I. Frenkel, N. Marinkovic, J. T. Muckerman, Y. Zhu and R. R. Adzic, *Angew. Chem. Int. Ed.*, 2012, **51**, 6131-6135.
67. B. Cao, G. M. Veith, J. C. Neuefeind, R. R. Adzic and P. G. Khalifah, *J. Am. Chem. Soc.*, 2013.
68. D. V. Sokolsky, V. S. Palanker and E. N. Baybatyrov, *Electrochim. Acta*, 1975, **20**, 71-77.
69. G. A. Tsirlina and O. A. Petrii, *Electrochim. Acta*, 1987, **32**, 649-657.
70. P. Zoltowski, *Electrochim. Acta*, 1980, **25**, 1547-1554.
71. R. D. Armstrong and M. F. Bell, *Electrochim. Acta*, 1978, **23**, 1111-1115.
72. I. Nikolov, T. Vitanov and V. Nikolova, *J. Power Sources*, 1980, **5**, 197-206.
73. I. Nikolov, K. Petrov, T. Vitanov and A. Guschev, *Int. J. Hydrogen Energy*, 1983, **8**, 437-440.
74. D. J. Ham, R. Ganesan and J. S. Lee, *Int. J. Hydrogen Energy*, 2008, **33**, 6865-6872.
75. F. Harnisch, G. Sievers and U. Schröder, *Appl. Catal., B*, 2009, **89**, 455-458.
76. E. J. Rees, K. Essaki, C. D. A. Brady and G. T. Burstein, *J. Power Sources*, 2009, **188**, 75-81.
77. A. T. Garcia-Esparza, D. Cha, Y. Ou, J. Kubota, K. Domen and K. Takanabe, *ChemSusChem*, 2013, **6**, 168-181.
78. Y. Zhao, K. Kamiya, K. Hashimoto and S. Nakanishi, *Angew. Chem. Int. Ed.*, 2013, **125**, 13883-13886.
79. S. Carenco, D. Portehault, C. Boissière, N. Mézailles and C. Sanchez, *Chem. Rev.*, 2013, **113**, 7981-8065.
80. S. T. Oyama, T. Gott, H. Zhao and Y.-K. Lee, *Catal. Today*, 2009, **143**, 94-107.
81. P. Liu, J. A. Rodriguez and J. T. Muckerman, *J. Phys. Chem. B*, 2004, **108**, 15662-15670.
82. Y. Xu, R. Wu, J. Zhang, Y. Shi and B. Zhang, *Chem. Commun.*, 2013, **49**, 6656-6658.
83. A. P. Raje and D. B. Dadyburjor, *Ind. Eng. Chem. Res.*, 1993, **32**, 1637-1644.
84. C. Di Giovanni, W.-A. Wang, S. Nowak, J.-M. Grenèche, H. Lecoq, L. Mouton, M. Giraud and C. Tard, *ACS catal.*, 2014, **4**, 681-687.
85. V. Schwartz, S. T. Oyama and J. G. Chen, *J. Phys. Chem. B*, 2000, **104**, 8800-8806.
86. C. C. Yu, S. Ramanathan, B. Dhandapani, J. G. Chen and S. T. Oyama, *J. Phys. Chem. B*, 1997, **101**, 512-518.

